

DualAnoDiff: Dual-Interrelated Diffusion Model for Few-Shot Anomaly Image Generation

Ying Jin^{1*}, Jinlong Peng^{2*}, Qingdong He^{2*}, Teng Hu³, Hao Chen¹, Jiafu Wu²,
Wenbing Zhu¹, Mingmin Chi^{1†}, Jun Liu², Yabiao Wang², Chengjie Wang²

¹Fudan University, ²Tencent Youtu Lab, ³Shanghai Jiaotong University
22210240186@m.fudan.edu.cn; {jeromepeng, yingcaihe}@tencent.com

Abstract

The performance of anomaly inspection in industrial manufacturing is constrained by the scarcity of anomaly data. To overcome this challenge, researchers have started employing anomaly generation approaches to augment the anomaly dataset. However, existing anomaly generation methods suffer from limited diversity in the generated anomalies and struggle to achieve a seamless blending of this anomaly with the original image. In this paper, we overcome these challenges from a new perspective, simultaneously generating a pair of the overall image and the corresponding anomaly part. We propose *DualAnoDiff*, a novel diffusion-based few-shot anomaly image generation model, which can generate diverse and realistic anomaly images by using a dual-interrelated diffusion model, where one of them is employed to generate the whole image while the other one generates the anomaly part. Moreover, we extract background and shape information to mitigate the distortion and blurriness phenomenon in few-shot image generation. Extensive experiments demonstrate the superiority of our proposed model over state-of-the-art methods in terms of both realism and diversity. Overall, our approach significantly improves the performance of downstream anomaly detection tasks, including anomaly detection, anomaly localization, and anomaly classification tasks. The code will be made available at <https://github.com/yinyjin/DualAnoDiff>.

Introduction

Industrial anomaly inspection, i.e., anomaly detection, localization, and classification, plays an important role in industrial manufacture (Duan et al. 2023). However, in real-world industrial production, anomaly samples are scarce. Therefore, the current mainstream anomaly inspection methods are either unsupervised methods which use only normal samples (Roth et al. 2022; Li et al. 2024b) or semi-supervised method (Zhang et al. 2023) which employ both the normal samples and a few anomaly data. Although these methods perform well in anomaly detection, they have limited performance in anomaly localization and can not deal with the task of anomaly classification (Hu et al. 2024). Therefore, researchers proposed anomaly generation methods to generate more anomaly data, to help achieve better performance by using supervised anomaly inspection.

*Equal contribution.

†Corresponding author.

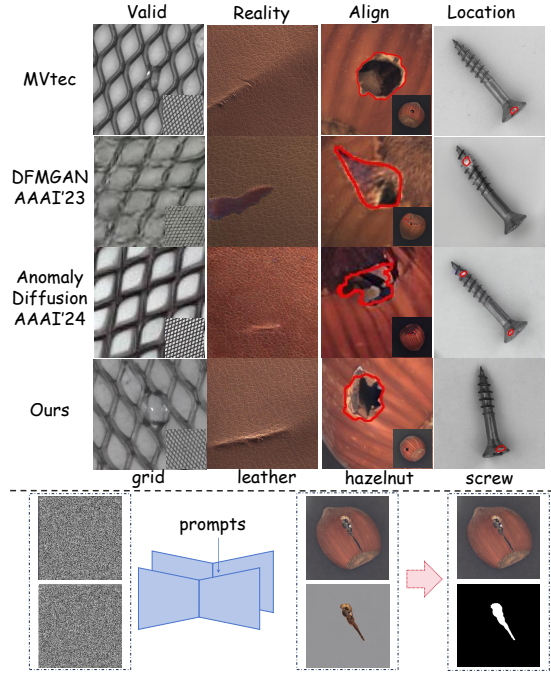


Figure 1: Top: Evaluating anomaly generation quality in four aspects: Whether generate valid anomaly, degree of realism, alignment of the mask, and whether the location of mask is reasonable, the results show that our generated results are better than the other methods. Bottom: Our model can simultaneously generate extensive anomaly image-mask pairs.

Existing anomaly generation methods can be categorized into two groups, 1) *model-free methods* randomly cut and paste patches from existing anomalies or anomalous texture datasets onto normal samples (Lin et al. 2021; Li et al. 2021). But the anomaly data synthesized by them is unrealistic. 2) *Generative methods* employ generative models like GANs and diffusion models to generate anomaly data. Generally, The GAN-based model (Zhang et al. 2021; Niu et al. 2020) requires a large amount of training data to achieve better generation performance and they can not generate masks. DFMGAN (Duan et al. 2023) firstly trained on normal data and then migrated to anomaly data to achieve a few shot generation. This method also encounters the problem that the generated anomalies are not realistic enough

(Peng et al. 2024) and the masks are not sufficiently aligned (Li et al. 2024a) because there is no explicit alignment constraint design. AnomalyDiffusion (Hu et al. 2024) based on the texture-inversion (Gal et al. 2022) technique of Diffusion (Rombach et al. 2022), separately learns the anomaly appearance and location information, then generates the anomaly on the masked normal samples. As AnomalyDiffusion only focuses on the part of anomaly, the generated anomalies do not blend realistically with the original image, and the masks generated individually may appear in the background of image.

To address these limitations, we propose DualAnoDiff, a novel few-shot anomaly image generation model that utilizes a dual-diffusion to simultaneously generate the overall image and the corresponding anomaly part. This approach can realize the effective integration of anomaly image and anomaly part, resulting in the generation of authentic and highly aligned anomaly image-mask data pairs. Specifically, our model is built upon a pre-trained diffusion model and introduces two LoRA to expand a single diffusion model into **dual-interrelated diffusion model**. One branch, referred to as the global branch, is responsible for generating the overall anomaly image, while the anomalous branch generates the localized anomaly image. They exchange information through the **self-attention interaction module**. This module combines the attention layers of global and anomalous branches and performs shared attention calculations, enabling the interaction and fusion of information in the dual-denoising process. This ensures the consistency between the generated overall anomaly image and the localized anomaly image. Furthermore, to further preserve the invariance of the background, we introduce a **background compensation module** based on self-attention adaptive injection. This module involves adding noise to the background image, extracting the key and value from the intermediate feature layer, and applying adaptive fusion MLP to incorporate the background information into the global branch. It helps to maintain consistency in the generated image and avoids coupling between the anomaly part and the background of the object in the image.

Fig. 1 shows our generation results outperform better compared with other method in four key aspects. Moreover, extensive experiments have been conducted in Mvtec AD (Bergmann et al. 2019) to quantitatively validate the superiority of the anomaly data generated by DualAnoDiff in downstream anomaly inspection tasks, and achieving a state-of-the-art level of performance with pixel-level **99.1% AU-ROC** and **84.5% AP** score.

Our contributions can be summarized as follows:

- We propose DualAnoDiff, a novel few-shot diffusion-based anomaly generation method, which simultaneously generates both the overall image and the corresponding anomaly part with a highly aligned mask by a dual-interrelated diffusion model.
- We design a background compensation approach, which involves image backgrounds as control information and injects the intermediate feature into the denoising process of anomaly image, to enhance the stability and authentic-

ity of the generated data.

- Extensive experiments demonstrate the superiority of our method over existing anomaly generation models in terms of both generation quality and performance of downstream anomaly inspection tasks.

Related Work

Few-shot Image Generation

Few-shot image generation aims to generate new and diverse examples while preventing overfitting to the few training images (Zhu et al. 2024). It is highly susceptible to overfit with extremely limited training data (less than 10) and then generate highly similar images. Early method (Mo, Cho, and Shin 2020) proposes modifying network weights, using various regularization techniques and data augmentation to prevent overfitting (Hu et al. 2024). There are also methods (Hu et al. 2023) to mitigate overfitting by pre-training on the source domain and subsequently migrating to fewer samples through cross-domain consistency losses to keep the generated distribution. Textual Inversion (Gal et al. 2022) and Dreambooth (Ruiz et al. 2023) encode a few images into the textual space of a pre-trained diffusion model to achieve diverse target customization generation which preserves its key visual features.

Anomaly Inspection

The anomaly inspection task consists of anomaly detection, localization, and classification (Duan et al. 2023). Due to the scarcity of abnormal data in industrial scenarios, most methods (Roth et al. 2022; Gu et al. 2024; Li et al. 2024b) use unsupervised methods and semi-supervised methods. Reconstruction-based methods (Schlegl et al. 2019; Cao et al. 2023; He et al. 2024) detect anomalies by analyzing the residual image before and after reconstruction. Embedding-based methods (Lee, Lee, and Song 2022; Cao et al. 2022; Wang et al. 2023b) utilize pre-trained networks to extract the image-level features and patch-level features, and then perform clustering according to the similarity between the features to detect the anomalies. All of those methods can only address the task of anomaly detection, while having limited performance in anomaly localization and being incapable of anomaly classification.

Anomaly Generation

Due to the scarcity of anomaly data, anomaly generation has emerged as a field of paramount importance. DRAEM (Zavrtanik, Kristan, and Skočaj 2021), Cut-Paste (Li et al. 2021), Crop-Paste (Lin et al. 2021) and PRN (Zhang et al. 2023) crop and paste unrelated textures or existing anomalies into normal sample. These approaches can be somewhat effective, but the generated anomalies are completely unrealistic and there is no way to use them as anomaly classification tasks. Subsequently, GANs (Goodfellow et al. 2020) have been applied for anomaly generation due to their ability to generate high-fidelity images. SDGAN (Niu et al. 2020) and DefectGAN (Zhang et al. 2021) generate anomalies

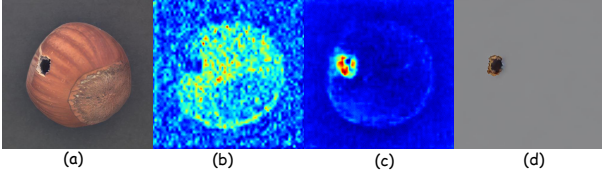


Figure 3: b, c are the cross attention maps of different text tokens in SD corresponding to the text of “a vfx with” and “sks”. a, d are the generated image from SD and SD*.

Dual-Interrelated Diffusion. AnomalyDiffusion (Hu et al. 2024) primarily focuses on the anomaly part, which may result in generated anomaly images lacking a convincingly realistic appearance. Directly generating the complete anomaly image poses challenges in obtaining the corresponding mask. To address those limitations, our proposed model simultaneously generates both the overall image and the anomaly part. This novel approach overcomes challenges in generating realistic anomaly images while ensuring the availability of accurate masks.

Firstly, we encode I, I_a into latent space $z, z' = \varepsilon(I), \varepsilon(I_a)$ by using VAE encoder $\varepsilon(\cdot)$, employ a forward process to add noise into the latents with the same timestep t , and then learn to denoising during the backward process guided by different prompts. Throughout these processes, information is shared and synchronized between the two diffusion models through the SAIM, enabling the model to effectively fit the training data pairs. By generating the anomalies separately, this approach achieves two important objectives. Firstly, it enhances the diversity and reality of the generated anomaly through a simple yet effective operation of adding two LoRA. Secondly, it ensures a highly aligned mask that accurately corresponds to the anomaly image.

Nested Prompts. The goal of the dual diffusion is to generate an anomaly image and anomaly part pair (I and I'), which exhibits an inclusion relationship. To facilitate the model’s understanding of the distinct entities within the image (the primary subject and the anomaly), we employ a pair of prompts designed to reflect this inclusion relationship:

$$\begin{aligned} p &: a \text{ x with } y \\ p' &: y \end{aligned} \quad (2)$$

where the prompts p and p' correspond to the anomaly image I and the corresponding anomaly part I_a respectively. Both prompts are encoded by the text encoder $\tau_\theta(\cdot)$ and then injected into Unet (Ronneberger, Fischer, and Brox 2015) of Diffusion. $\tau_\theta(\cdot)$ is trainable.

The variables x and y can be the class name and anomaly name provided by the dataset. In our model, we use the *vfx* and *sks* which were suggested by DreamBooth (Ruiz et al. 2023). Those words have weak prior in both the language model and the diffusion model, making them easier to fit than other words, and can achieve better generation results, specially for high-prior words. Fig. 3 presents the generated result and visualizes the cross-attention maps between text token and vision. where a, d are the anomaly image and anomaly part generated by SD and SD^* . b and c are the 64×64 resolutions feature maps randomly extracted from the second half of the generation process in the U-Net of



Figure 4: Comparison between the models without (a) and with (b) the Background Compensation Module

SD . Where b corresponds to the text “a vfx with”, c corresponds to “sks”. It is evident that the model correctly separates the attributes of anomaly and object, and accurately associating them to the specified text as we want.

Self-attention Interaction Module (SAIM). During training, SD and SD^* share the same timestep t and denoising simultaneously, they share information after every attention in the unet. For example, self-attention is more likely to share the positional information and cross-attention shares the semantic information. The shared step is formulated as:

$$\begin{aligned} \varphi_i(\tilde{z}) &= Rearrange(Concat(\varphi_i(z), \varphi_i(z'))) \\ \varphi_i(\tilde{z})_{new} &= SelfAtt(\varphi_i(\tilde{z})) \\ \varphi_i(z), \varphi_i(z') &= Split(Rearrange(\varphi_i(\tilde{z})_{new} + \varphi_i(\tilde{z}))) \end{aligned} \quad (3)$$

where φ^i is the intermediate representation of the U-Net. The original shape of $\varphi_i(z)$ and $\varphi_i(z')$ are “b w c”, where b denotes the batch size, w represents the spatial dimension, and c represents the channel dimension. We rearrange the $concat(\varphi_i(z), \varphi_i(z'))$ to shape of “bw 2 c”. Concat and split are a set of corresponding operations that are used to aggregate and separate $varphi_i(z), \varphi_i(z')$.

Loss Function. With the two-stream parallel structure of diffusion, our final training objective expressed as follows:

$$\begin{aligned} \mathcal{L} &= \mathbb{E}_{\mathcal{E}(I), \epsilon, t} [\|\epsilon - \epsilon_\theta(z_t, t, \tau_\theta(p))\|_2^2] \\ &+ \mathbb{E}_{\mathcal{E}(I_a), \epsilon^*, t} [\|\epsilon^* - \epsilon_\theta^*(z'_t, t, \tau_\theta(p'))\|_2^2] \end{aligned} \quad (4)$$

here, ϵ and ϵ^* are latent noise for the anomaly image and anomaly part, t is the time step, p, p' are the corresponding prompts, they are encoded by text encoder $\tau_\theta(\cdot)$ which is trainable.

Mask Generation. Thanks to our two-stream parallel structure, which generates the anomaly part as a single entity, obtaining the precise mask becomes straightforward. There are two ways to obtain a high-quality mask. Firstly, we can utilize existing segmentation algorithms such as SAM (Kirillov et al. 2023), U²-Net (Qin et al. 2020) to obtain high-quality masks after generating the anomaly part image. Additionally, during the generation process, we can extract the average attention maps in SD^* to compute the mask such as (Wang et al. 2023a) which is widely used in semantic segmentation. In our paper, we use the first method.

Category	CDC		Crop-Paste		SDGAN		Defect-GAN		DFMGAN		AnomalyDiffusion		Ours	
	IS \uparrow	IC-L \uparrow	IS \uparrow	IC-L \uparrow	IS \uparrow	IC-L \uparrow	IS \uparrow	IC-L	IS \uparrow	IC-L \uparrow	IS \uparrow	IC-L \uparrow	IS \uparrow	IC-L \uparrow
bottle	1.52	0.04	1.43	0.04	1.57	0.06	1.39	0.07	<u>1.62</u>	0.12	1.58	0.19	2.17	0.36
cable	1.97	0.19	1.74	0.25	1.89	0.19	1.70	0.22	1.96	0.25	2.13	<u>0.41</u>	<u>2.12</u>	0.43
capsule	1.37	0.06	1.23	0.05	1.49	0.03	<u>1.59</u>	0.04	<u>1.59</u>	0.11	<u>1.59</u>	<u>0.21</u>	1.60	0.31
carpet	<u>1.25</u>	0.03	1.17	0.11	1.18	0.11	1.24	0.12	1.23	0.13	1.16	<u>0.24</u>	1.36	0.29
grid	1.97	0.07	2.00	0.12	1.95	0.10	2.01	0.12	1.97	0.13	<u>2.04</u>	0.44	2.09	<u>0.42</u>
hazel_nut	<u>1.97</u>	0.05	1.74	0.21	1.85	0.16	1.87	0.19	1.93	0.24	2.13	<u>0.31</u>	1.91	0.35
leather	1.80	0.07	1.47	0.14	2.04	0.12	2.12	0.14	<u>2.06</u>	<u>0.17</u>	1.94	0.41	1.88	<u>0.34</u>
metal_nut	1.55	0.04	<u>1.56</u>	0.15	1.45	0.28	1.47	<u>0.30</u>	1.49	0.32	1.96	0.30	<u>1.56</u>	0.32
pill	1.56	0.06	1.49	0.11	1.61	0.07	1.61	0.10	<u>1.63</u>	0.16	1.61	<u>0.26</u>	1.82	0.37
screw	1.13	0.11	1.12	0.16	1.17	0.10	1.19	0.12	1.12	0.14	<u>1.28</u>	<u>0.30</u>	1.34	0.36
tile	2.10	0.12	1.83	0.20	<u>2.53</u>	0.21	2.35	0.22	2.39	0.22	2.54	0.55	2.35	<u>0.50</u>
toothbrush	1.63	0.06	1.30	0.08	1.78	0.03	<u>1.85</u>	0.03	1.82	0.18	1.68	<u>0.21</u>	2.40	0.48
transistor	1.61	0.13	1.39	0.15	1.76	0.13	1.47	0.13	1.64	0.25	1.57	0.34	<u>1.69</u>	<u>0.33</u>
wood	2.05	0.03	1.95	0.23	2.12	0.25	2.19	0.29	2.12	0.35	2.33	<u>0.37</u>	<u>2.21</u>	0.40
zipper	1.30	0.05	1.23	0.11	1.25	0.10	1.25	0.10	1.29	0.27	<u>1.39</u>	<u>0.25</u>	2.09	0.36
Average	1.65	0.07	1.51	0.14	1.71	0.13	1.69	0.15	1.72	0.20	<u>1.80</u>	<u>0.32</u>	1.90	0.37

Table 1: Comparison on IS and IC-LPIPS on MVTec dataset. Our model generates the most high-quality and diverse anomaly data, achieving the best IS and IC-LPIPS. Bold and underline represent optimal and sub-optimal results, respectively.

Background Compensation Module

Although the model has achieved good results so far, there are still some problems in some cases, which is caused by the limited training data. Several bad cases of corresponding generated results are shown in Fig. 4 for categories bottle, pill, and toothbrush in the Mvtec (the average training data for each category is 8). The bottle was only partially generated. The edges of pill is blurred and the internal properties leakage into the background. Additionally, the toothbrush has two brush handles, which is an abnormal occurrence. Furthermore, all of those generated images lack sharpness and the background color does not maintain sufficient purity. In general, the model is incapable of fully grasping the characteristics of those cases, there are problems such as objects and background mixed, and objects deformed.

To enhance the model’s ability to learn the shape of object and focus more on object generation, we design a background compensation module. First, We employ U²-Net to segment the image I and obtain the object mask M_f , then get the background image $I_b = (1 - M_f) \times I$, I_b will process the SD as same as I (except for the SAIM). Next, We utilize I_b as a condition, which contains both background and mask information. This allows us to control the shape of the object while providing background context. We collect its features in self-attentions and inject them into the K , V of the I in every corresponding self-attention steps. The injection process can be formulated as:

$$\begin{aligned}
\varphi_i(z^b) &= SelfAtt(\varphi_i(z^b)) \\
Q &= W_Q^{(i)} \cdot \varphi_i(z) \\
\varphi_i(z) &= \varphi_i(z) + \gamma MLP(\varphi_i(z^b)) \\
K &= W_K^{(i)} \cdot \varphi_i(z) \quad V = W_V^{(i)} \cdot \varphi_i(z)
\end{aligned} \tag{5}$$

where γ is a learnable scale factor initialized to be 0.1. This design can help us to maximally preserve the generative effect of the mainstream SD, meanwhile use background information and the shape of the mask. With the condition of

I_b , the loss function becomes:

$$\begin{aligned}
\mathcal{L} &= \mathbb{E}_{\mathcal{E}(I), \epsilon, t} \left[\|\epsilon - \epsilon_\theta(z_t, t, \tau_\theta(p), I_b)\|_2^2 \right] \\
&+ \mathbb{E}_{\mathcal{E}(I), \epsilon^*, t} \left[\|\epsilon^* - \epsilon_\theta^*(z'_t, t, \tau_\theta(p'), I_b)\|_2^2 \right]
\end{aligned} \tag{6}$$

Experiments

Experiment Settings

Dataset. we conduct experiments on MVTec (Bergmann et al. 2019). We refer to the experimental setup of Anomaly-Diffusion (Hu et al. 2024) using 1/3 of the data as the training set, reserving the remaining two-thirds for testing. **Implementation details.** We train a model for each anomaly type separately and generate 500 anomaly image-mask pairs for the downstream anomaly inspection tasks. More details of the experiment can be found in the supplementary materials. **Metric. 1) For generation,** we use Inception Score (IS) and Intra-cluster pairwise LPIPS distance (IC-LPIPS) (Ojha et al. 2021) as AnomalyDiffusion (Hu et al. 2024) to measure the generation quality and generation diversity. **2) For anomaly inspection.** We use AUROC, Average Precision (AP), and the F1-max score to evaluate the accuracy of anomaly detection and localization.

Comparison in Anomaly Generation

Baseline. 1) We select DRAEM(Zavrtanik, Kristan, and Skočaj 2021), PRN (Zhang et al. 2023), DFMGAN (Duan et al. 2023) and AnomalyDiffusion (Hu et al. 2024) which can generate anomaly image-mask pairs as comparative benchmarks to compare anomaly detection and localization. 2) We choose CDC (Ojha et al. 2021), Crop-Paste, SDGAN (Niu et al. 2020), DefectGAN (Zhang et al. 2021), DFMGAN (Duan et al. 2023) and AnomalyDiffusion (Hu et al. 2024) that can only generate specific anomaly types to compare anomaly generation quality and classification.

Category	DRAEM				PRN				DFMGAN				AnomalyDiffusion				Ours			
	AUC-P	AP-P	F1-P	AP-I	AUC-P	AP-P	F1-P	AP-I	AUC-P	AP-P	F1-P	AP-I	AUC-P	AP-P	F1-P	AP-I	AUC-P	AP-P	F1-P	AP-I
bottle	96.7	80.2	74.0	99.8	97.5	76.4	71.3	98.4	98.9	90.2	83.9	99.8	99.4	94.1	87.3	99.9	99.5	93.4	85.7	100
cable	80.3	21.8	28.3	83.2	94.5	64.4	61.0	92.0	97.2	81.0	75.4	97.8	99.2	90.8	83.5	100	<u>97.5</u>	<u>82.6</u>	<u>76.9</u>	<u>98.3</u>
capsule	76.2	25.5	32.1	98.7	95.6	45.7	47.9	95.8	79.2	26.0	35.0	98.5	<u>98.8</u>	<u>57.2</u>	<u>59.8</u>	99.9	99.5	73.2	67.0	<u>99.2</u>
carpet	92.6	43.0	41.9	98.7	96.4	69.6	65.6	97.8	90.6	33.4	38.1	98.5	<u>98.6</u>	<u>81.2</u>	<u>74.6</u>	98.8	99.4	89.1	80.2	99.9
grid	99.1	59.3	58.7	99.9	<u>98.9</u>	<u>58.6</u>	58.9	98.9	75.2	14.3	20.5	90.4	98.3	52.9	54.6	99.5	98.5	57.2	54.9	<u>99.7</u>
hazelnut	98.8	73.6	68.5	100	98.0	73.9	68.2	96.0	<u>99.7</u>	95.2	89.5	100	99.8	<u>96.5</u>	<u>90.6</u>	<u>99.9</u>	99.8	97.7	92.8	100
leather	98.5	67.6	65.0	100	99.4	58.1	54.0	99.7	98.5	68.7	66.7	100	99.8	<u>79.6</u>	<u>71.0</u>	100	99.9	88.8	78.8	100
metal_nut	96.9	84.2	74.5	99.6	97.9	93.0	87.1	99.5	99.3	<u>98.1</u>	94.5	99.8	99.8	98.7	<u>94.0</u>	100	<u>99.6</u>	98.0	93.0	<u>99.9</u>
pill	95.8	45.3	53.0	98.9	98.3	55.5	72.6	97.8	81.2	67.8	72.6	91.7	99.8	97.0	90.8	99.6	<u>99.6</u>	<u>95.8</u>	<u>89.2</u>	<u>99.0</u>
screw	91.0	30.1	35.7	<u>96.3</u>	94.0	47.7	49.8	94.7	58.8	2.2	5.3	64.7	97.0	<u>51.8</u>	<u>50.9</u>	97.9	98.1	57.1	56.1	95.0
tile	98.5	93.2	87.8	100	98.5	91.8	84.4	<u>96.9</u>	<u>99.5</u>	97.1	91.6	100	99.2	<u>93.9</u>	86.2	100	99.7	97.1	<u>91.0</u>	100
toothbrush	93.8	29.5	28.4	<u>99.8</u>	96.1	46.4	46.2	100	96.4	<u>75.9</u>	<u>72.6</u>	100	99.2	76.5	73.4	100	<u>98.2</u>	68.3	68.6	99.7
transistor	76.5	31.7	24.2	80.5	94.9	68.6	68.4	88.9	96.2	81.2	77.0	92.5	99.3	92.6	85.7	100	<u>98.0</u>	86.7	79.6	93.7
wood	98.8	<u>87.8</u>	<u>80.9</u>	100	96.2	74.2	67.4	92.7	95.3	70.7	65.8	99.4	<u>98.9</u>	84.6	74.5	99.4	99.4	91.6	83.8	<u>99.9</u>
zipper	93.4	65.4	64.7	100	98.4	79.0	73.7	99.7	92.9	65.6	64.9	<u>99.9</u>	99.4	<u>86.0</u>	<u>79.2</u>	100	99.6	90.7	82.7	100
Average	92.2	54.1	53.1	97.0	<u>96.9</u>	66.2	64.7	96.6	90.0	62.7	62.1	94.8	99.1	<u>81.4</u>	<u>76.3</u>	99.7	99.1	84.5	78.8	<u>98.9</u>

Table 2: Comparison on pixel-level and image-level anomaly localization on MVtec dataset by training an U-Net on the generated data from DRAEM, PRN, DFMGAN, AnomalyDiffusion and our model.

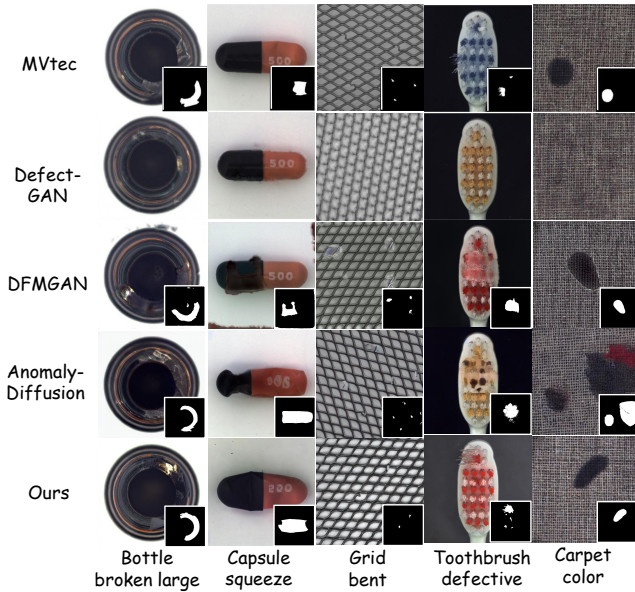


Figure 5: Comparison of the generation results on MVtec. Our model excels in generating high-quality anomaly images that are accurately aligned with the anomaly masks.

Anomaly Generation Quality. Tab. 1 shows the results of the quantification metrics for image quality. For each anomaly category, we allocate one-third of the anomaly data for training and generate 500 anomaly images to compute IS and IC-LPIPS. It demonstrates that our model generates anomaly data with both the highest quality and diversity.

Moreover, we present the anomaly images generated by several prominent anomaly image generation models in Fig. 5, among which, AnomalyDiffusion is by far the state-of-the-art method. It is observed that the images generated by DefectGAN often do not have anomalies, DFMGAN tends to introduce noise in the image, and the anomaly image-mask pairs lack proper alignment. The state-of-the-art model Anomaly-

Category	DiffAug	Crop-Paste	DFMGAN	AnoDiff	Ours
bottle	48.84	52.71	56.59	90.70	76.74
cable	21.36	32.81	45.31	67.19	71.88
capsule	34.67	32.8	37.23	<u>66.67</u>	70.67
carpet	35.48	27.96	47.31	<u>58.06</u>	74.19
grid	28.33	28.33	40.83	<u>42.50</u>	80.0
hazelnut	65.28	59.03	81.94	<u>85.42</u>	89.58
leather	40.74	34.39	49.73	<u>61.90</u>	90.48
metalnut	58.85	59.89	64.58	<u>59.38</u>	82.81
pill	29.86	26.74	29.52	59.38	<u>54.17</u>
screw	25.10	28.81	37.45	<u>48.15</u>	70.37
tile	59.65	68.42	74.85	<u>84.21</u>	100
transistor	38.09	41.67	52.38	<u>60.71</u>	67.86
wood	41.27	47.62	49.21	<u>71.43</u>	85.71
zipper	22.76	26.42	27.64	69.51	69.51
Average	39.31	40.55	49.61	<u>66.09</u>	72.26

Table 3: Comparison on anomaly classification accuracy trained on the generated data by the anomaly generation models with a ResNet-18.

Diffusion may generate an unreasonable mask that is outside the object, and the generated anomaly does not fit the original image enough to make the anomaly look unreal. In contrast, our proposed model demonstrates the ability to generate highly realistic and valid anomalies, even excelling in handling smaller-scale anomalies such as grid-bent. More results are presented in the supplementary material.

Anomaly Generation for Anomaly Detection and Localization. we evaluate the effectiveness of our approach by comparing it with existing methods for anomaly generation in downstream anomaly detection and localization. We calculate pixel-level dimensions and image-level AUROC, AP, and F1-max for each category. The results are presented in Tab. 2, and because the image-level results of AUROC, AP, and F1-max are relatively similar, as well as the limitation of the table width, we only show the results of the most representative AP, and the other results of AUROC and F1-max are shown in the supplementary material. It can be seen that

Category	Unsupervised						Supervised			
	DRAEM	SSPCAB	CFA	RD4AD	PatchCore	Musc	DevNet	DRA	PRN	Ours
bottle	99.1/88.5	98.9/88.6	98.9/50.9	98.8/51.0	97.6/75.0	98.5/82.8	96.7/67.9	91.7/41.5	99.4/92.3	99.5/93.4
cable	94.8/61.4	93.1/52.1	98.4/79.8	98.8/77.0	96.8/65.9	96.2/58.8	97.9/67.6	86.1/34.8	98.8/78.9	97.5/82.6
capsule	97.6/47.9	90.4/48.7	98.9/71.1	99.0/60.5	98.6/46.6	98.9/52.7	91.1/46.6	88.5/11.0	98.5/62.2	99.5/73.2
carpet	96.3/62.5	92.3/49.1	99.1/47.7	99.4/46.0	98.7/65.0	99.4/75.3	94.6/19.6	98.2/54.0	99.0/82.0	99.4/89.1
grid	99.5/53.2	99.6/58.2	98.6/82.9	98.0/75.4	97.2/23.6	98.6/37.0	90.2/44.9	86.2/28.6	98.4/45.7	98.5/57.2
hazelnut	99.5/88.1	99.6/94.5	98.5/80.2	94.2/57.2	97.6/55.2	99.3/74.4	76.9/46.8	88.8/20.3	99.7/93.8	99.8/97.7
leather	98.8/68.5	97.2/60.3	96.2/60.9	96.6/53.5	98.9/43.4	99.7/62.6	94.3/66.2	97.2/ 5.1	99.7/69.7	99.9/88.8
metal_nut	98.7/91.6	99.3/95.1	98.6/74.6	97.3/53.8	97.5/86.8	87.5/49.6	93.3/57.4	80.3/30.6	99.7/98.0	99.6/98.0
pill	97.7/44.8	96.5/48.1	98.8/67.9	98.4/58.1	97.0/75.9	97.6/65.6	98.9/79.9	79.6/22.1	99.5/91.3	99.6/95.8
screw	99.7/72.9	99.1/62.0	98.7/61.4	99.1/51.8	98.7/34.2	98.9/31.7	66.5/21.1	51.0/5.1	97.5/44.9	98.1/57.1
tile	99.4/96.4	99.2/96.3	98.6/92.6	97.4/78.2	94.9/56.0	98.3/80.6	88.7/63.9	91.0/54.4	99.6/96.5	99.7/97.1
toothbrush	97.3/49.2	97.5/38.9	98.4/61.7	99.0/63.1	97.6/37.1	99.4/64.2	96.3/52.4	74.5/4.8	99.6/78.1	98.2/68.3
transistor	92.2/56.0	85.3/36.5	98.6/82.9	99.6/50.3	91.8/66.7	92.5/61.2	55.2/4.4	79.3/11.2	98.4/85.6	98.0/86.7
wood	97.6/81.6	97.2/77.1	97.6/25.6	99.3/39.1	95.7/54.3	98.7/77.5	93.1/47.9	82.9/21.0	97.8/82.6	99.4/91.6
zipper	98.6/73.6	98.1/78.2	95.9/53.9	99.7/52.7	98.5/63.1	98.4/64.2	92.4/53.1	96.8/42.3	98.8/77.6	99.6/90.7
Average	97.7/69.0	96.2/65.5	98.3/66.3	98.3/57.8	97.1/56.6	97.5/62.6	86.4/49.3	84.8/25.7	99.0/78.6	99.1/84.5

Table 4: Comparison on pixel-level anomaly localization (AUROC/AP) between the simple U-Net trained on our generated dataset and the existing anomaly detection methods with their official codes or pre-trained models.

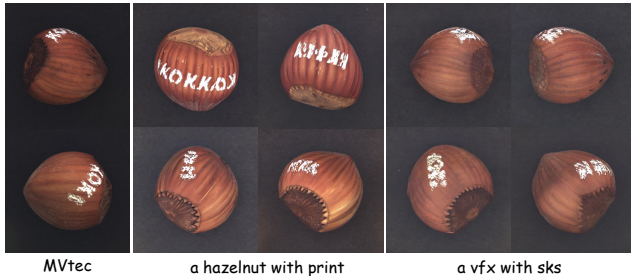


Figure 6: Comparison of generation results for different prompts on the hazelnut-print category.

the U-net trained in our generated data reaches the highest AP of **84.5%** and F1-max of **78.8%**, surpassing the second-ranked AnomalyDiffusion by a margin of **3.1% (AP)**.

Anomaly Generation for Anomaly Classification. To further assess the quality of the anomaly images generated by our model, we utilize them to train a downstream anomaly classification model. Following the experimental setup of DFMGAN (Duan et al. 2023), we employ ResNet-34 to train on the generated dataset. We then evaluate the classification accuracy on our test dataset as shown in Tab. 3. As evident from the data, our model demonstrates significantly higher accuracy across the majority of categories compared to other models, with an average accuracy improvement of **6.17%**, indicating the anomaly data we generate is more realistic.

Comparison with Anomaly Detection Models

To further validate the effectiveness of our model, we compare it with state-of-the-art anomaly detection methods DRAEM(Zavrtanik, Kristan, and Skočaj 2021), SSP-CAB (Ristea et al. 2022), CFA (Lee, Lee, and Song 2022), RD4AD (Deng and Li 2022), PatchCore (Roth et al. 2022), MuSc (Li et al. 2024b), DevNet (Pang et al. 2021), DRA (Ding, Pang, and Shen 2022) and PRN (Zhang et al. 2023). We utilize their official codes or pre-trained models and evaluate them on the same testing dataset (2/3 anomaly data in the test of Mvtec). As there is no available open-source code

Category	Without BCM			With BCM		
	AUROC	AP	F1-max	AUROC	AP	F1-max
bottle	98.4	88.8	77.1	99.5	93.4	85.7
pill	98.4	86.9	78.2	99.6	95.8	89.2
toothbrush	97.2	62.7	64.0	98.2	68.3	68.6
Average	98.8	83.0	78.1	99.1	84.5	78.8

Table 5: Comparison on pixel-level anomaly localization on part of categories in MVtec between with/without the Background Compensation Module. Average is the mean of all categories in Mvtec.

for PRN, we rely on the data provided in its research paper. The methods are evaluated based on their pixel-level AUROC and AP scores, as demonstrated in Tab. 4.

Ablation Study

Fig. 6 presents the results of using different prompts in our model. It is evident that using the prompt “a vfx with sks” yields superior performance in terms of object shape, color, and other aspects compared to using the category name directly. More quantitative indicators can be found in the supplementary material. Furthermore, we assess the effectiveness of the Background Compensation Module (BCM), which exhibits more noticeable improvements in the categories of bottle, pill, and toothbrush. The visualization results are depicted in Fig. 4, and the pixel-level localization results are presented in Tab. 5.

Conclusion

In this paper, we present a novel approach, DualAnoDiff, for generating anomalous image-mask pairs. Our method employs a parallel dual-diffusion to simultaneously generate the anomaly image and the corresponding anomaly part image. This ensures a high level of alignment between the generated anomaly image-mask pair and the authenticity of the anomaly. Additionally, to address challenging cases, we in-

roduce a background compensation module that efficiently enhances the model’s fitting capability. Extensive experiments demonstrate its superior performance compared to existing anomaly generation methods. The anomaly data generated by our model effectively enhances the performance of downstream anomaly inspection tasks.

References

- Bergmann, P.; Fauser, M.; Sattlegger, D.; and Steger, C. 2019. MVTec AD—A comprehensive real-world dataset for unsupervised anomaly detection. In *CVPR*, 9592–9600.
- Cao, Y.; Wan, Q.; Shen, W.; and Gao, L. 2022. Informative knowledge distillation for image anomaly segmentation. *Knowledge-Based Systems*, 248: 108846.
- Cao, Y.; Xu, X.; Sun, C.; Cheng, Y.; Du, Z.; Gao, L.; and Shen, W. 2023. Segment Any Anomaly without Training via Hybrid Prompt Regularization. *arXiv preprint arXiv:2305.10724*.
- Deng, H.; and Li, X. 2022. Anomaly detection via reverse distillation from one-class embedding. In *CVPR*, 9737–9746.
- Ding, C.; Pang, G.; and Shen, C. 2022. Catching both gray and black swans: Open-set supervised anomaly detection. In *CVPR*, 7388–7398.
- Duan, Y.; Hong, Y.; Niu, L.; and Zhang, L. 2023. Few-Shot Defect Image Generation via Defect-Aware Feature Manipulation. In *AAAI*, volume 37, 571–578.
- Gal, R.; Alaluf, Y.; Atzmon, Y.; Patashnik, O.; Bermano, A. H.; Chechik, G.; and Cohen-Or, D. 2022. An image is worth one word: Personalizing text-to-image generation using textual inversion. *arXiv preprint arXiv:2208.01618*.
- Goodfellow, I.; Pouget-Abadie, J.; Mirza, M.; Xu, B.; Warde-Farley, D.; Ozair, S.; Courville, A.; and Bengio, Y. 2020. Generative adversarial networks. *Communications of the ACM*, 63(11): 139–144.
- Gu, Z.; Zhang, J.; Liu, L.; Chen, X.; Peng, J.; Gan, Z.; Jiang, G.; Shu, A.; Wang, Y.; and Ma, L. 2024. Rethinking Reverse Distillation for Multi-Modal Anomaly Detection. In *Proceedings of the AAAI Conference on Artificial Intelligence*, volume 38, 8445–8453.
- He, L.; Jiang, Z.; Peng, J.; Liu, L.; Du, Q.; Hu, X.; Zhu, W.; Chi, M.; Wang, Y.; and Wang, C. 2024. Learning Unified Reference Representation for Unsupervised Multi-class Anomaly Detection. In *Proceedings of the European Conference on Computer Vision*.
- Hu, E. J.; Shen, Y.; Wallis, P.; Allen-Zhu, Z.; Li, Y.; Wang, S.; Wang, L.; and Chen, W. 2021. Lora: Low-rank adaptation of large language models. *arXiv preprint arXiv:2106.09685*.
- Hu, T.; Zhang, J.; Liu, L.; Yi, R.; Kou, S.; Zhu, H.; Chen, X.; Wang, Y.; Wang, C.; and Ma, L. 2023. Phasic Content Fusing Diffusion Model with Directional Distribution Consistency for Few-Shot Model Adaption. In *Proceedings of the IEEE/CVF International Conference on Computer Vision*, 2406–2415.
- Hu, T.; Zhang, J.; Yi, R.; Du, Y.; Chen, X.; Liu, L.; Wang, Y.; and Wang, C. 2024. Anomalydiffusion: Few-shot anomaly image generation with diffusion model. In *Proceedings of the AAAI Conference on Artificial Intelligence*, volume 38, 8526–8534.
- Karras, T.; Laine, S.; Aittala, M.; Hellsten, J.; Lehtinen, J.; and Aila, T. 2020. Analyzing and improving the image quality of stylegan. In *CVPR*, 8110–8119.
- Kingma, D. P.; and Welling, M. 2013. Auto-encoding variational bayes. *arXiv preprint arXiv:1312.6114*.
- Kirillov, A.; Mintun, E.; Ravi, N.; Mao, H.; Rolland, C.; Gustafson, L.; Xiao, T.; Whitehead, S.; Berg, A. C.; Lo, W.-Y.; et al. 2023. Segment anything. In *Proceedings of the IEEE/CVF International Conference on Computer Vision*, 4015–4026.
- Lee, S.; Lee, S.; and Song, B. C. 2022. Cfa: Coupled-hypersphere-based feature adaptation for target-oriented anomaly localization. *IEEE Access*, 10: 78446–78454.
- Li, C.-L.; Sohn, K.; Yoon, J.; and Pfister, T. 2021. Cutpaste: Self-supervised learning for anomaly detection and localization. In *CVPR*, 9664–9674.
- Li, P.; Nie, Q.; Chen, Y.; Jiang, X.; Wu, K.; Lin, Y.; Liu, Y.; Peng, J.; Wang, C.; and Zheng, F. 2024a. Tuning-free image customization with image and text guidance. In *Proceedings of the European Conference on Computer Vision*.
- Li, X.; Huang, Z.; Xue, F.; and Zhou, Y. 2024b. Musc: Zero-shot industrial anomaly classification and segmentation with mutual scoring of the unlabeled images. *arXiv preprint arXiv:2401.16753*.
- Lin, D.; Cao, Y.; Zhu, W.; and Li, Y. 2021. Few-shot defect segmentation leveraging abundant defect-free training samples through normal background regularization and crop-and-paste operation. In *ICME*, 1–6. IEEE.
- Mo, S.; Cho, M.; and Shin, J. 2020. Freeze the discriminator: a simple baseline for fine-tuning gans. *arXiv preprint arXiv:2002.10964*.
- Niu, S.; Li, B.; Wang, X.; and Lin, H. 2020. Defect image sample generation with GAN for improving defect recognition. *IEEE Transactions on Automation Science and Engineering*, 17(3): 1611–1622.
- Ojha, U.; Li, Y.; Lu, J.; Efros, A. A.; Lee, Y. J.; Shechtman, E.; and Zhang, R. 2021. Few-shot image generation via cross-domain correspondence. In *CVPR*, 10743–10752.
- Pang, G.; Ding, C.; Shen, C.; and Hengel, A. v. d. 2021. Explainable deep few-shot anomaly detection with deviation networks. *arXiv preprint arXiv:2108.00462*.
- Peng, J.; Luo, Z.; Liu, L.; and Zhang, B. 2024. Frih: Fine-grained region-aware image harmonization. In *Proceedings of the AAAI Conference on Artificial Intelligence*, volume 38, 4478–4486.
- Qin, X.; Zhang, Z.; Huang, C.; Dehghan, M.; Zaiane, O. R.; and Jagersand, M. 2020. U2-Net: Going deeper with nested U-structure for salient object detection. *Pattern recognition*, 106: 107404.
- Radford, A.; Kim, J. W.; Hallacy, C.; Ramesh, A.; Goh, G.; Agarwal, S.; Sastry, G.; Askell, A.; Mishkin, P.; Clark, J.; et al. 2021. Learning transferable visual models from natural language supervision. In *International conference on machine learning*, 8748–8763. PMLR.

Ristea, N.-C.; Madan, N.; Ionescu, R. T.; Nasrollahi, K.; Khan, F. S.; Moeslund, T. B.; and Shah, M. 2022. Self-supervised predictive convolutional attentive block for anomaly detection. In *CVPR*, 13576–13586.

Rombach, R.; Blattmann, A.; Lorenz, D.; Esser, P.; and Ommer, B. 2022. High-resolution image synthesis with latent diffusion models. In *Proceedings of the IEEE/CVF conference on computer vision and pattern recognition*, 10684–10695.

Ronneberger, O.; Fischer, P.; and Brox, T. 2015. U-net: Convolutional networks for biomedical image segmentation. In *Medical image computing and computer-assisted intervention—MICCAI 2015: 18th international conference, Munich, Germany, October 5-9, 2015, proceedings, part III 18*, 234–241. Springer.

Roth, K.; Pemula, L.; Zepeda, J.; Schölkopf, B.; Brox, T.; and Gehler, P. 2022. Towards total recall in industrial anomaly detection. In *CVPR*, 14318–14328.

Ruiz, N.; Li, Y.; Jampani, V.; Pritch, Y.; Rubinstein, M.; and Aberman, K. 2023. Dreambooth: Fine tuning text-to-image diffusion models for subject-driven generation. In *CVPR*, 22500–22510.

Schlegl, T.; Seeböck, P.; Waldstein, S. M.; Langs, G.; and Schmidt-Erfurth, U. 2019. f-AnoGAN: Fast unsupervised anomaly detection with generative adversarial networks. *Medical image analysis*, 54: 30–44.

Wang, J.; Li, X.; Zhang, J.; Xu, Q.; Zhou, Q.; Yu, Q.; Sheng, L.; and Xu, D. 2023a. Diffusion model is secretly a training-free open vocabulary semantic segmenter. *arXiv preprint arXiv:2309.02773*.

Wang, Y.; Peng, J.; Zhang, J.; Yi, R.; Wang, Y.; and Wang, C. 2023b. Multimodal industrial anomaly detection via hybrid fusion. In *Proceedings of the IEEE/CVF Conference on Computer Vision and Pattern Recognition*, 8032–8041.

Zavrtanik, V.; Kristan, M.; and Skočaj, D. 2021. Draem-a discriminatively trained reconstruction embedding for surface anomaly detection. In *ICCV*, 8330–8339.

Zhang, G.; Cui, K.; Hung, T.-Y.; and Lu, S. 2021. Defect-GAN: High-fidelity defect synthesis for automated defect inspection. In *Proceedings of the IEEE/CVF Winter Conference on Applications of Computer Vision*, 2524–2534.

Zhang, H.; Wu, Z.; Wang, Z.; Chen, Z.; and Jiang, Y.-G. 2023. Prototypical residual networks for anomaly detection and localization. In *CVPR*, 16281–16291.

Zhang, L.; and Agrawala, M. 2024. Transparent image layer diffusion using latent transparency. *arXiv preprint arXiv:2402.17113*.

Zhu, J.; Ma, H.; Chen, J.; and Yuan, J. 2024. High-Quality and Diverse Few-Shot Image Generation via Masked Discrimination. *IEEE Transactions on Image Processing*.